

A pragmatic approach for the numerical prediction of meteotsunamis in Ciutadella harbour (Balearic Islands)

R. Romero^{*}, M. Vich, C. Ramis

Grup de Meteorologia, Departament de Física, Universitat de les Illes Balears, Ctra. de Valldemossa km. 7.5, Palma de Mallorca 07122, Spain

ABSTRACT

Ciutadella (Menorca, Balearic Islands, Spain) is well known for the large amplitude seiches of about 10.5 min period registered in its long and narrow inlet, especially during the warm season. This phenomenon, locally referred to as “rissaga”, might reach extreme wave heights (in the range 1.5 – 4 m) with a recurrence of only a few years, leading to damaging consequences in the port activities and moored vessels. The provision of as accurate as possible predictions of the rissaga risk, hours or days ahead, appears as a crucial element in helping to mitigate these consequences.

We devise a chain of atmospheric and oceanic numerical simulation components aimed at capturing with low computational cost the key physical processes conducive to the vast majority of rissaga events: (i) the genesis upstream from the Balearic Islands of high amplitude atmospheric gravity waves travelling in the SW–NE direction; these mesoscale waves are synthetically triggered using a 2D nonhydrostatic fully compressible model within a vertical environment provided by a representative sounding; (ii) the oceanic response to the concomitant pressure fluctuations along the Menorca channel, in the form of long oceanic waves subject to Proudman resonance; these processes are simulated with a shallow-water model applied over a 80-m depth channel; (iii) shelf amplification, which according to theory (Green’s law) accounts for a doubling of the wave amplitude for a depth jump from 80 to 5 m; and (iv) harbour resonance within Ciutadella inlet, a crucial mechanism solved again with the shallow-water equations over the idealized 5-m deep channel.

The prognostic system is successfully tested for the available set of 126 rissaga events and for a complementary set of 549 ordinary situations. Our approach discriminates fairly well non-rissaga events from high-amplitude oscillations and tends to correctly categorize the meteotsunamis among weak, moderate or strong events. We are now pursuing the real time application of the method in a probabilistic context.

1. Introduction and physical mechanisms

Meteotsunamis or atmospherically induced high-frequency sea level variations (oscillation periods in the range of minutes; Monserrat et al., 2006) are known to have hit coasts all around the world, especially in bays with high amplification factor or narrow harbours where the local seiches can more easily resonate with the external forcing and develop large amplitudes (Rabinovich, 2009). Wherever and whenever this phenomenon interacts with humans, it will pose a hazard to our activities (Pattiaratchi and Wijeratne, 2015). Destructive meteotsunamis, i.e. with effects comparable to their seismic counterparts, are certainly exceptional and seem to be the result of optimal combinations of atmospheric sources of appropriate – in both amplitude and time scale – sea level pressure fluctuations, with resonant mechanisms unfolded during the oceanic phase of the episode. As for most of extreme phenomena of natural origin, it is the geographical context (and notably in this case the topographies of the sea floor and coastal feature) what determines the meteotsunami prone areas globally. One of such places is the Ciutadella harbour in Menorca (Balearic Islands, Spain), right in the centre of the western Mediterranean sea (Ramis and Jansà, 1983; Rabinovich and Monserrat, 1998).

During most active years Ciutadella will experience several rissaga¹ events of about 100 cm wave height (crest-to-trough difference), with

oscillation periods close to 10.5 min; this is the fundamental period of the seiche in a long-narrow, rectangular and semiclosed basin (Wilson, 1972) with the characteristics of Ciutadella harbour (1.1 km length, 80 m width and 5 m depth, see Fig. 1). In extreme cases (on average every 5–10 years) these oscillations can reach several metres, like the event of 15 June 2006, with 400 cm wave height, the most violent manifestation of a rissaga reported during the last decades (Jansà et al., 2007), closely followed by the meteotsunami of 21 June 1984 (350 cm). In this sense, Ciutadella readily competes with other singular territories where this kind of extreme atmospherically induced ocean waves in the tsunami frequency band have also been reported: e.g. Nagasaki Bay (Japan) with its *Abiki* phenomenon (Hibiya and Kajiura, 1982), and the vast, geographically complex eastern Adriatic coast of Croatia, historically impinged by several destructive meteotsunamis (Vilibić and Šepić, 2009); (for a more general context of the problem see Adams-Selin and Johnson, 2010 and Pattiaratchi and Wijeratne, 2015). Obviously, the strong currents induced by even moderate oscillations of sea level within the Ciutadella harbour become highly disruptive for the normal operations of the port. In the most severe cases, like the June 1984 and June 2006 events, in only 5 min the state of the port switches between a dry bed near the closed end of the harbour, and enormous water levels that flood contiguous areas and break moorings, leaving

^{*} Corresponding author.

E-mail address: romu.romero@uib.es (R. Romero).

¹ *Rissaga* is the local name for a meteotsunami in Ciutadella. The phenomenon is most common during the warm season (May to September).

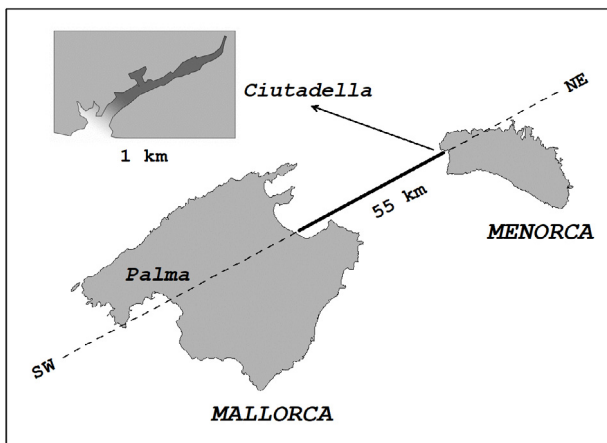


Fig. 1. Depiction of Mallorca and Menorca (northern sector of the Balearics Islands). Atmospheric radiosounding station is located in Palma (the capital of the archipelago). The top-left inset is a close-up view of Ciutadella harbour, where the meteotsunamis occur. SW-NE oriented lines (including the harbour itself) reflect the three domains for the numerical simulations (see text for details)

the vessels adrift. Any step towards a better prediction of the rissaga phenomenon has the potential to help anticipating these effects hours or days in advance and thus the adoption of proportional measures of protection.

The fundamental processes leading to meteotsunami generation over the Mediterranean and Black Sea regions were nicely illustrated by Šepić et al. (2015). The chain of atmospheric-oceanic mechanisms (see the well-known Fig. 4 of that paper) is certainly applicable to the majority of rissaga events. First, pressure fluctuations of enough entity (a few hPa) and short time periods (several minutes) are generated at sea level via the tropospheric ducting of internal gravity waves (Lindzen and Tung, 1976; Monserrat and Thorpe, 1996). For the trapping and propagation of these waves without significant vertical energy loss and dissipation, an upward transition in a highly sheared environment from a layer with large static stability (even with a thermal inversion) to steep mid-tropospheric lapse rates, becomes necessary. In these circumstances, an unstable atmospheric layer (in terms of the Richardson number, $Ri < 0.25$) that might contain a critical (steering) level, will overlie a stable layer ($Ri > 0.25$) and the surface manifestation of the atmospheric gravity waves would take the form of noticeable pressure variations. For the specific case of Ciutadella, the required basic current and strong unidirectional wind shear across the tropospheric column should be preferentially from the W-SW direction, as this is the orientation of the inlet (Fig. 1). At synoptic scale, all the previous conditions are linked to the presence of a relatively cold upper-level trough to the west of the Balearics, simultaneous with (or shortly preceded by) a weak circulation from the southern sector at low levels that brings a surge of warm African air and a strong temperature inversion over the western Mediterranean waters (Ramis and Jansà, 1983). In fact, the surveillance of such synoptic pattern, most frequent during the warm season, forms the basis of an empirically based rissaga warning system currently operational at the national weather service of Spain (AEMET). The reliability of these warnings improves for the short term when clear signals of gravity wave activity can be confirmed on satellite images (i.e. propagation of elongated southwesterly plumes of cloud bands aligned in the transverse direction), although quantitative estimations of the possible rissaga generally remain elusive. A real example of a perfect combination of atmospheric ingredients, as observed by the regional sounding launched at Palma de Mallorca station (100 km upstream from Menorca, see Fig. 1), is shown in Fig. 2 for the June 1984 event.

Rapid sea level atmospheric oscillations, sometimes lasting several hours, might include singular pressure jumps in response to more

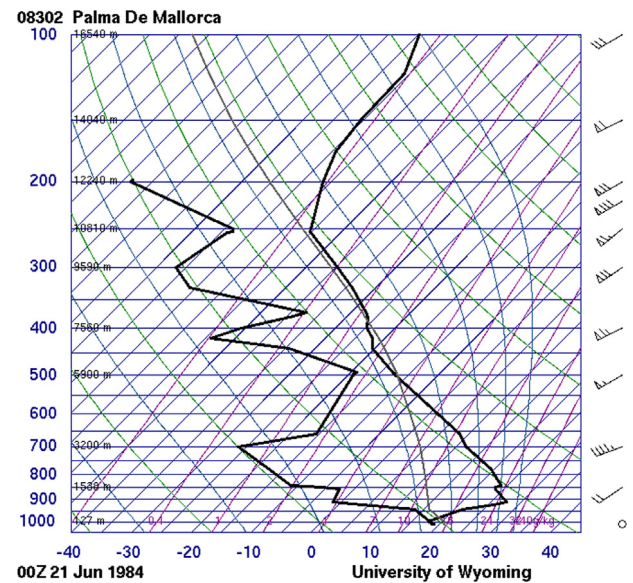


Fig. 2. Radiosounding data from Palma de Mallorca on 21 June 1984 at 00 UTC. The large scale ingredients for rissaga generation are clearly identified in these profiles: (i) strong vertical wind shear affecting the basic south-westerly current and (ii) presence of very warm air around 850 hPa (and cold air at mid-tropospheric levels) that induces an abrupt change of stability in the vertical.

intense phases of gravity wave activity (Paxton and Sobien, 1998). Or such pressure jumps are simply the consequence of other kinds of meteorological disturbances (Jansà et al., 2007), e.g. the northeastward propagation of a mesoscale convective system (MCS), including small squall lines, a crucial element for some of the largest sea level oscillations observed in Ciutadella. The role of MCS surface pressure anomalies as a trigger of meteotsunamis has been exhaustively documented in other places thanks to the continuous information provided by rich observing systems (e.g. for the June 13th, 2013 events along the US East Coast; Wertman et al., 2014; Bailey et al., 2014) to the point that an early warning of MCS-generated tsunamis is revealed as a feasible task wherever a detailed monitoring of these anomalies is possible with the available data. In our experience, the occasional formation of a MCS during rissaga situations is just another symptom of the occurrence of greatly amplified gravity waves. Specifically, for the abovementioned record-breaking event of 15 June 2006, where the passage of a MCS with its characteristic pressure jump during the evening was crucial (Jansà et al., 2007), atmospheric gravity waves and moderate sea level oscillations of around 100 cm had been observed all day long; the air mass evolved from thermodynamic and kinematic profiles at the beginning of the day similar to those shown in Fig. 2, into an afternoon environment with greatly reduced convective inhibition and large CAPE (aprox. 2000 J/kg) for the parcels located right above the inversion (soundings not shown), thus allowing the gravity waves to release this convective energy.

Equilibrium response to surface pressure variations of only a few hPa cannot directly explain large oscillations of the sea level; inverted barometer principle would account for an equivalent of nothing more than few centimetres. Anomalously amplified harbour seiches at Ciutadella are known to be mainly associated with the external forcing provided by long ocean waves travelling northeastward in the open sea between Mallorca and Menorca (Ramis and Jansà, 1983; Marcos et al., 2009). These waves (with periods predominantly in the range of 5–50 min) are driven by the atmospheric disturbance, but in order to become effective they must gain enough amplitude when impinging on the mouth of the harbour. The previous conceptual model by Šepić et al. (2015) emphasizes the Proudman resonance (Proudman, 1929) and shelf amplification (due to shoaling; Green, 1838) as the leading

mechanisms for this crucial stage of the phenomenon. Proudman resonance is due to the matching of the long ocean waves speed (25–30 m s⁻¹ for a depth of about 80 m between the islands) and the propagation speed of the precursor atmospheric gravity wave. Shoaling effects for a depth transition from 80 m in the channel to 5 m of the harbour, would mean doubling the wave amplitude according to Green's law. Together, both mechanisms could feasibly build ocean wave amplitudes of several tens of cm after the ≈50 km path separating the islands (Fig. 1) and to practically 1 m in most extreme cases.

Finally, the last and most evident step of the Šepić et al. (2015) physical scheme for a rissaga generation is the harbour resonance, due to matching of the frequency of incoming long ocean waves and harbour eigenperiods. Periods close to the fundamental mode of 10.5 min will generally be the most effective for generating rissagas in Ciutadella. Under an optimal sequence of the outlined atmosphere–ocean processes in terms of their attributes (amplitudes, frequencies and propagation speeds), incoming ocean waves can be amplified more than 100 times before hitting Ciutadella coast, entailing a destructive meteotsunami.

In principle, a modelling system suited for quantitative rissaga forecasts will need some type of formulation of the above generation mechanisms and their complex interactions. For the ocean, a simple shallow-water model, for instance, may suffice to represent the dynamics and amplification of the long ocean waves, provided the atmospheric coupling and resonant mechanisms are accounted for. The inclusion of several kinds of resonances in semi idealized numerical frameworks is uncomplicated and has been exploited profusely in the literature in order to analyse the role of these processes in real systems: e.g. with one of such models, Vennell (2010) investigates the resonance and trapping of topographic transient ocean waves by prescribing a moving atmospheric disturbance; Bubalo et al. (2018) simulates Chrystal and Proudman resonances in a closed rectangular basin with two finite element and one finite difference ocean models; and Vilibić (2008) designs numerical modelling exercises with various sinusoidal air pressure disturbances to reproduce the Proudman resonance on a shelf, drawing illuminating conclusions about the genesis of destructive meteotsunami events. Regarding the atmospheric component of the modelling system, realistic representations of internal gravity waves (or other precursor atmospheric disturbances) is more demanding but it is also practicable with a good investment in resolution and appropriate versions of the primitive nonlinear hydrodynamic equations (e.g. Stephan et al., 2016).

In this work we devise a pragmatic (and computationally inexpensive) numerical approach aimed at predicting the occurrence and magnitude of meteotsunamis in Ciutadella harbour. The idea is to retain exclusively the physical mechanisms pointed out by Šepić et al. (2015) and the consideration of contexts as simple as possible (e.g. initialization with a single radiosounding and use of 2D geometries and flat bottom topography). The method involves the application of the nonhydrostatic fully compressible equations for the atmospheric part and the adaptation of the shallow water equations to simulate the oceanic response. We propose this strategy (for the moment for a dry atmosphere) as an effective and affordable method that avoids the application of full 3D high-resolution atmosphere–ocean coupled models, where meteotsunami generation processes are supposed to emerge and combine naturally. That is the case, specifically, of the sophisticated SOCIB/BRIFS rissaga forecasting system² operational at the Balearic Islands; the system was described and successfully tested for the June 2006 meteotsunami event by Renault et al. (2011); last years' experience with BRIFS reveals its good skill to recognize rissaga situations but a clear tendency to underestimate the wave height (A. Jansà, personal communication).

² See <http://www.socib.es/index.php?seccion=modelling&facility=rissagaforecast>.

The characteristics of our three-step methodology are described in Section 2: in first place, we present the atmospheric component responsible for the generation and propagation of gravity waves (2.1); in second place, the Menorca channel submodel, aimed at driving the long ocean waves and their possible amplification via Proudman and shoaling processes (2.2); and finally, the model application to Ciutadella inlet in order to incorporate the harbour resonance mechanism (2.3). Key features of the new construct will be illustrated with reference to the 21 June 1984 case study, that is, through the results obtained after feeding the technique with the environmental characteristics of the sounding of Fig. 2. In Section 3 we summarize the statistical performance of the prognostic system, based on its application to the available set of historical rissaga events and to a contrasting collection of non-rissaga days (Section 3.1); Section 3.2 outlines its skill when it comes to differentiating categories of practical interest. Finally, Section 4 will contain the main conclusions of the study and some hints for short and mid-term research.

2. Methodology description: 21 June 1984 case study

2.1. Atmospheric component (gravity wave generation)

The atmospheric model of our prognostic system uses one of the traditional equation sets that govern the dynamics of a nonhydrostatic fully compressible atmosphere (see Giraldo and Restelly, 2008). In two dimensions (x, z) these equations are written as:

$$\begin{aligned}\frac{\partial \pi'}{\partial t} &= -u \frac{\partial \pi'}{\partial x} - w \frac{\partial \pi'}{\partial z} - w \frac{\partial \bar{\pi}}{\partial z} - \frac{R}{c_p} (\bar{\pi} + \pi') \left[\frac{\partial u}{\partial x} + \frac{\partial w}{\partial z} \right] \\ \frac{\partial \theta'}{\partial t} &= -u \frac{\partial \theta'}{\partial x} - w \frac{\partial \theta'}{\partial z} - w \frac{\partial \bar{\theta}}{\partial z} \\ \frac{\partial u}{\partial t} &= -u \frac{\partial u}{\partial x} - w \frac{\partial u}{\partial z} - c_p (\bar{\theta} + \theta') \frac{\partial \pi'}{\partial x} \\ \frac{\partial w}{\partial t} &= -u \frac{\partial w}{\partial x} - w \frac{\partial w}{\partial z} - c_p (\bar{\theta} + \theta') \frac{\partial \pi'}{\partial z} + g \frac{\theta'}{\bar{\theta}}\end{aligned}$$

where besides the tendencies for the wind in the vertical plane (u, w), predictive equations for Exner pressure and potential temperature perturbations (π', θ') appear. These perturbations are defined with respect to a reference state, indicated with overbars, that depends on height only and is in hydrostatic balance. In addition to the inviscid flow conditions that define the above form of the Euler equations, our simplified atmosphere is dry and adiabatic. That is, no other physical processes (explicit or parameterized) apart from basic hydro- and thermo-dynamics, are formulated³. Note we also omit Coriolis and curvature terms. In summary, all these possible influences are considered irrelevant, or at least of second order, for gravity wave-driven rissaga events.

From the initial conditions, the system of equations is integrated using a forward-in-time splitting method (e.g. Wicker and Skamarock, 1998), that is, using two time levels and considering a large time step for the horizontal and vertical advection “slow” terms, and a short time step for the other terms appearing on the right side of the equations. The formulation of these latter “fast” terms uses standard second-order finite difference spatial operators and, in time, applies a forward–backward scheme (mass equations are updated first, then followed by wind equations) that proceeds through an intermediate point of the short time interval, according to a second-order Runge–Kutta (RK2) cycle (a thorough review of the concepts and benefits of these numerical strategies can be found in Durran (2010)).

³ Truly speaking, some amount of mixing of the prognostic fields is implicitly incorporated in the solution owing to the numerical formulation of the advective terms (see text). Explicit diffusion terms (or filters) are not needed in our model to guarantee a good behaviour of the numerical solution.

Regarding the advection terms, these are integrated over the large time step (typically 6–10 times longer than previous Δt) in the rectangular (x, z) grid following a Reconstruct-Evolve-Average (REA) philosophy, inspired by the finite volume methods point of view (see [Leveque, 2002](#)). Specifically, a REA algorithm with piecewise linear reconstruction is applied in the vertical direction and then in the horizontal (dimensional splitting) as follows: (i) for each grid cell (segment), a linear profile of the field is reconstructed using the central grid point value and an adequate choice for the slope or gradient in that direction (R step); (ii) this profile evolves conservatively (i.e. the segment is translated along the corresponding direction and possibly stretches/shrinks) by the action of the velocity components found at segment edges (E step); and (iii) the new grid point values resulting from the advection process are calculated by averaging within the cell limits all segments (i.e. their profiles) that totally or partially remained or entered the cell (A step). Note we do not apply any type of staggering of variables in our model, that is, all prognostic fields (u, w, π', θ') are defined at the same grid points; as consequence, wind components at segment edges necessary for the E step are approximated using the two contiguous cells.

What exactly defines the numerical behaviour of the REA scheme is the particular choice of the slope for the R step. For instance, a zero slope yields a scheme equivalent to the first order upwind method, known for correctly preserving the monotonicity of the solution but inducing an unacceptable degree of dissipation. Slopes consistent with popular second (or higher) order methods can also be defined, but then other characteristic problems of these schemes, like phase error and oscillatory contamination of the solution, can easily emerge. The previous pathologies can be greatly reduced by using slope limiter methods (a synonym term for the flux limiting strategy distinctive of the high-resolution finite volume methods, [Leveque, 2002](#)). Among the large family of these specially defined — and local solution dependent — slopes, and guided by several advection tests (not shown), we found the monotonized central-difference limiter (MC limiter; [Van Leer, 1977](#)) as the most suitable choice.

Additionally, we allow in our model a vertical stretching of the grid cells with the purpose of placing more resolution at low levels, where it is needed to properly resolve the complexities of the thermal structure (e.g. the sharp vertical gradients of stability seen in the sounding of [Fig. 2](#)). But the use of too short Δz would severely restrict the maximum time step compatible with numerical stability. In order to circumvent this problem, acoustic vertical modes linked to $\partial_z w$ and $\partial_z \pi'$ terms in the first and last equations, respectively, are stabilized with an implicit formulation of these derivatives in the finite difference form of the temporal integration. This is a common practice in numerical codes of elastic models (e.g. [Skamarock et al., 2008](#)) and basically means that the CFL criterion behind the maximum allowable time step will now be determined exclusively in terms of the horizontal grid length Δx .

We subjected our model to several benchmark tests found in the literature. Some of these tests involve the simulation of thermal bubbles. As an example, [Fig. 3a](#) shows the same four stages of the exercise proposed by [Robert \(1993\)](#), regarding the interaction of a rising large warm bubble and a descending small cold bubble introduced in a calm and neutrally-stable environment. Times shown are 0, 4, 7 and 10 min, as in [Fig. 9](#) of the above paper. Another well-known test is a density current simulation initialized with a strong cold anomaly embedded in the same kind of environment ([Straka et al., 1993](#)). Our [Fig. 3b](#) shows again the θ' evolution (half domain only) at exactly the same moments of the Straka et al. experiment (0, 5, 10 and 15 min, compare with their [Fig. 1](#)). Our model also passed mountain wave tests after activating a topographic bottom boundary condition and a gravity wave absorbing layer towards the upper troposphere and above (Rayleigh damping term added to w equation, ([Klemp et al., 2008](#)). The [Schär et al. \(2002\)](#) test, for instance, analyses the stationary response of a uniform westerly current (10 m s^{-1}) with constant stratification (Brunt–Väisälä frequency $N = 0.01 \text{ s}^{-1}$) to the presence of a 250 m-height mountain possessing an

analytical profile composed of a bell-shaped envelope combined with shorter scale cosine-shaped components (see [Fig. 3c](#), where the w field is shown with a contour interval of $\pm 0.05 \text{ m s}^{-1}$). The solution for this mountain wave is very interesting as it contains a mixture of a larger-scale hydrostatic wave with deep propagation in the vertical, and smaller-scale nonhydrostatic waves rapidly decaying with height. This output can be directly compared with other model simulations and with the analytical solution (see [Fig. 13](#) of [Schär et al., 2002](#)). Our final illustrative example deals with the simulation of an intense mountain wave excited by Sierra Nevada range (CA, USA) under the impingement of a flow that is initialized using a real upstream sounding, taken during the T-REX observational campaign ([Doyle et al., 2011](#)). Nonlinearities and transient features are highly influential in this case and no stationary state is reached, but persistent features in this simulation ([Fig. 3d](#)) are the downslope windstorm conditions and hydraulic jump found at low levels, along the eastern slope, and the profound wave breaking occurring aloft. These structures have been represented after 4 h of simulation exactly in the same way as in the model intercomparison composite contained in [Fig. 5](#) of [Doyle et al. \(2011\)](#): black contours display the potential temperature field at intervals of 10 K, and colour indicates the horizontal perturbation wind component (interval of $+5 \text{ m s}^{-1}$ and -5 m s^{-1} for red and blue areas, respectively). Based on these and several other comparison exercises, including tests with the three-dimensional version of the code, we can easily conclude that our model performs at least as well as state-of-the-art modelling systems.

With regard to the specific application to the rissaga problem, the model is initialized with a horizontally homogeneous basic state $(\bar{\pi}, \bar{\theta}, \bar{u})$ imported from the “representative” Palma sounding ([Fig. 2](#) for the case study) and runs for a 12 h period. The simulation uses a non-orographic domain extended along the relevant direction (namely, the SW–NE axis oriented 30° with respect to the zonal direction, dashed line in [Fig. 1](#)); thus the sounding winds are first projected along such direction to build the initial u profile. To avoid any spurious contamination of the results with boundary artefacts, our model includes a proper scheme for the relaxation of the inner solution towards the basic state imposed at the lateral boundaries ([Davies and Turner, 1977](#)). In addition, we use a long enough domain of 300 km; Ciutadella lies at the central point of this length. In the vertical the domain extends till 20 km height. The horizontal resolution is $\Delta x = 300 \text{ m}$ while in the vertical it varies gradually from $\Delta z = 20 \text{ m}$ at sea level to 180 m at the uppermost computational layers. A critical issue of the method is how to excite the gravity waves in the simulation so as to allow the environmental characteristics (shear and stability profiles) to govern their downstream propagation, amplification or dissipation. Triggering mechanisms that are naturally ubiquitous in the real atmosphere are absent in our highly synthetic and simplified context. We found an effective way of introducing the atmospheric disturbances in the domain by resorting to the left boundary condition for the w field: a gaussian-shaped vertical profile of downward motion (centred at a height of 8 km with a maximum of -8.5 m s^{-1} and possessing a full width at half maximum of 6 km) is continuously forced along that boundary during the simulation. This type of triggering function, focused on the mid-upper troposphere, is inspired by the observations of atmospheric jets as preferred sources of internal gravity waves (e.g. [Plougonven and Zhang, 2014](#)). Mutual adjustment of mass and wind prognostic fields as this perturbation enters the domain is all what is needed to develop a significant gravity wave response, unless the basic environment found downstream is hostile. Admittedly, this perturbation technique is rather arbitrary and the maximum downdraft value, especially, can be considered a free (or calibration) parameter of our modelling system. In our specific case we experimented with a range of values, approximately at intervals of $\pm 0.5 \text{ m s}^{-1}$; global results in terms of mean simulated wave height for 126 analysed rissaga events were found to be optimal (i.e. closest to observations, see [Section 3.1](#)) when using -8.5 m s^{-1} . Future improvements of the technique could incorporate the individual characteristics of the synoptic situation and use a different parameter

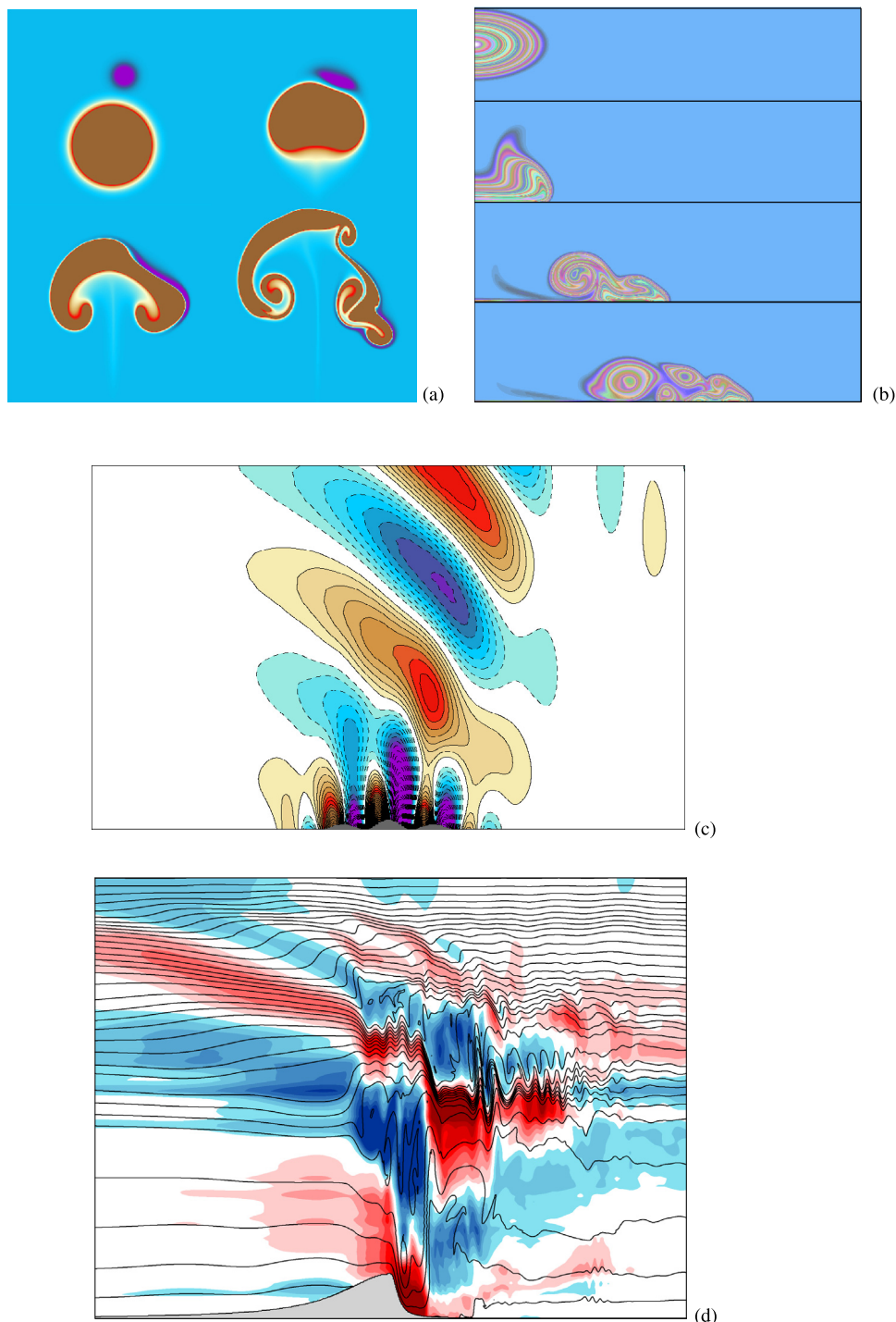


Fig. 3. Validation tests of the atmospheric model: (a) Interaction of a large warm bubble and a small cold bubble (Robert, 1993); (b) Density current (Straka et al., 1993); (c) Schär mountain wave (Schär et al., 2002); (d) T-REX Intense Mountain-Wave (Doyle et al., 2011).

for each day; for instance, the parameter could be scaled according to the amount of flow imbalance associated with the upper level jet, since many different studies have consistently highlighted jet exit regions (where this imbalance tends to be maximized) as a favoured locus for intense gravity waves (see Plougonven and Zhang, 2014).

A graphical representation of the atmospheric gravity wave resulting for our case study is included in Fig. 4a, that shows the total potential temperature field ($\bar{\theta} + \theta'$) at 5 h of simulation. In agreement with the physical scheme described in the previous section, the most remarkable features of this result are the lack of dissipation of the disturbance as it propagates downstream (from left to right in the

figure) and the notable amplitude of the wave near the surface, where it is needed to properly interact with the underlying water body. The crucial role of both wind and temperature vertical profiles for enabling the previous features can be easily demonstrated by repeating the numerical experiment after altering these profiles. For instance, Fig. 4b shows a simulation initialized with a uniform wind along the z axis (i.e. no shear), namely the vertically averaged value of the sounding wind data; the disturbance rapidly decays both in the vertical and horizontal dimensions. On the other hand, Fig. 4c results from an environment possessing the same wind as the reference sounding of Fig. 2 but this time assuming a temperature profile similar to the standard

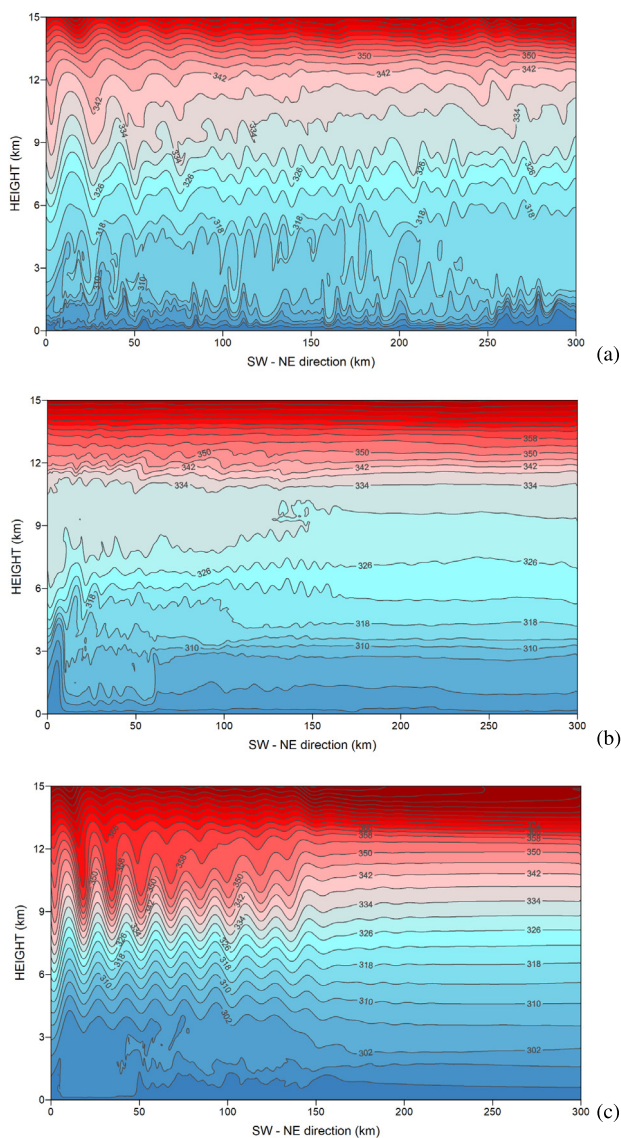


Fig. 4. Potential temperature field (contour interval is 4 K) corresponding to the atmospheric model simulation of 21 Jun 1984 case study at $t = 5$ h using: (a) Original sounding (Fig. 2); (b) Constant mean wind in the vertical; (c) Standard atmosphere temperature profile.

atmosphere (a lapse rate of 6 K/km is applied in the troposphere, isothermal conditions above); in this case the gravity waves remain practically confined to the mid-upper troposphere and no appreciable signatures (in short, pressure fluctuations) are revealed at surface.

2.2. Menorca channel (Proudman resonance & wave shoaling)

The second step in the meteotsunami generation scheme of Šepić et al. (2015) involves a favourable atmosphere–ocean coupling in the Menorca channel. The channel was unequivocally demonstrated by Ličer et al. (2017) to be the key build-up region determining meteotsunami amplitude in Ciutadella. Looking at the travelling sea level pressure (SLP) fluctuations provided by the previous simulation of the 21 June 1984 case study, several promising features are observed in the surface wave (these features are practically absent under the modified environments of Fig. 4b and c). First of all, the resulting pressure wave possesses a significant amplitude, of about 2 hPa (the SLP time series at the south-western limit of the channel is displayed in Fig. 5a). In second place, the oscillating nature of the signal, with a dominant

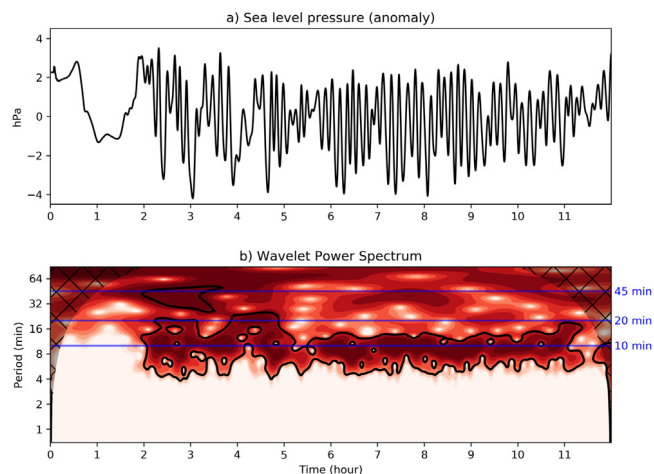


Fig. 5. Atmospheric model simulation of 21 Jun 1984 case study: (a) Time series of the sea level pressure signal obtained at the entrance of Menorca channel (100 km point in Fig. 4a); (b) Wavelet power spectrum of the SLP series (indicated periods of 10, 20 and 45 min, in blue, locate approximately the main energy maxima found in the global wavelet spectrum, not shown).

period in the range of minutes, becomes evident; at the location of Fig. 5a, for instance, it can be seen that after the initial two hours (when the disturbance has not yet arrived) a quasi-regular pattern of pressure variations is established. Leaving aside the non-linear influences, these characteristic periodicities are exclusively an intrinsic property of the background environment where the gravity waves are embedded, not an artificial consequence of the method (note, in particular, we do not impose any oscillatory character or time dependency in the above described GW triggering function). The characteristics of the SLP signal can be better analysed through its Wavelet transform (Fig. 5b). This tool captures the change in frequency response with respect to time and is especially useful to analyse transients, aperiodicities and other non-stationary signal features (e.g. Kelley, 2018). In this case we use the Morlet Wavelet transform and show only the energy scalogram, which gives the relative importance of different periods at the selected location; in Fig. 5b the bold black contour highlights the frequency regions where the power is significant (power/noise ratio significant at level 95). The Wavelet power spectrum clearly indicates that the surface image of the gravity-wave activity is most intense for periods around 10 min, precisely the optimum for Ciutadella inlet. Additional peaks of energy content at about 20 and 45 min are also delineated during some phases of the 21 June 1984 simulation (Fig. 5b). As expected, similar analyses to Fig. 5 but for the no-shear and standard-atmosphere runs (graphics not shown), not only reveal pressure fluctuations of much less amplitude, but also quite different distributions of the energy across the spectral bands (no apparent peaks, for instance, appear near the 10 min optimum).

Finally, the propagation speed of the SLP wave should be examined, as this represents the most crucial factor for the amplification of the forced ocean waves via Proudman resonance. A rough estimate of this speed over the domain of interest can be obtained by searching the time lag that maximizes the correlation between the SLP series simulated at both sides of Menorca channel (we use the 100 km and 150 km points of Fig. 4a for this purpose). The temporal evolution of the propagation speed so calculated is shown in Fig. 6. Note that this speed is continuously fluctuating in spite of starting from horizontally homogeneous conditions and maintaining the same initial sounding at the lateral boundaries; this is due to the strong non-linear interactions among the spatially-complex atmospheric disturbances (Fig. 4a) and the background state. Based only on Fig. 6, we can identify several phases of the simulation exhibiting a north-eastward translation of the SLP wave across the channel faster than 20 m s^{-1} , but it is the

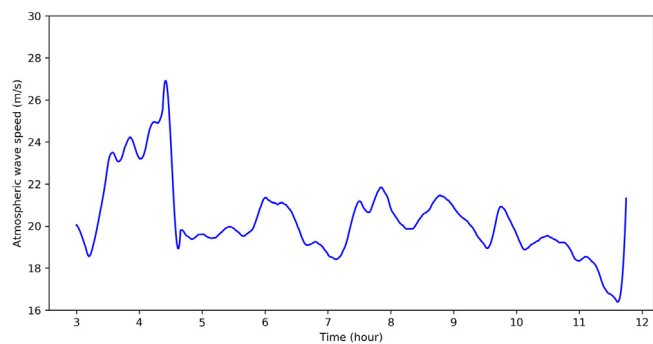


Fig. 6. Atmospheric model simulation of 21 Jun 1984 case study: Propagation speed of the SLP “wave” along the Menorca channel. This speed is estimated according to the maximum time-lagged correlation between the SLP time series at 100 km point (shown in Fig. 5a) and that at the 150 km point (not shown).

maximum obtained shortly after 4 h of simulation time (propagation speeds in the range 25–30 m s⁻¹) what emerges as the best scenario for Proudman-type intensification of the long ocean waves.

In our simplified approach, the nonlinear oceanic response in the Menorca channel is numerically quantified by means of the shallow water equations⁴ after inclusion of the appropriate atmospheric forcing term:

$$\begin{aligned}\frac{\partial h}{\partial t} &= -u \frac{\partial h}{\partial x} - h \frac{\partial u}{\partial x} \\ \frac{\partial u}{\partial t} &= -u \frac{\partial u}{\partial x} - g \frac{\partial h}{\partial x} - \frac{1}{\rho} \frac{\partial P}{\partial x} - \frac{gu^2}{hC^2}\end{aligned}$$

Predictive equations for water depth (h) and velocity (u) are solved for the 55 km long Mallorca-Menorca stretch (Fig. 1) using a horizontal resolution $\Delta x = 600$ m and non-reflecting boundary conditions. Initially, the channel is assumed to have a uniform depth of 80 m (i.e. flat bottom topography, a good approximation for the Menorca channel given its smooth relief) and to be at rest. The oceanic component is connected with the atmospheric system through the pressure forcing term affecting the second equation (P is the time and space varying sea level pressure provided by the atmospheric simulation every 20 s; sea density ρ is set at 1028 kg m⁻³). Similarly to Vilibić (2008) we also include in the momentum equation a drag force, where the seabed frictional resistance C is defined as $C = 18 \log_{10}(0.37 h/z_0)$, with the bottom roughness z_0 set at 0.003 m. No additional terms like Coriolis and wind-driven forces are considered as these are assumed to be of second-order importance for our problem. Diffusion is acting implicitly in the simulation as part of the advection scheme.

The numerical scheme used to solve the coupled equations is analogous to the procedure followed for the atmospheric model, except for the time splitting which is not applied in this case. Specifically, we also follow a RK2 implementation of the two-time level scheme, with a forward-backward second order formulation of mass and wind terms, and REA representation of advection; pressure forcing and drag terms are simply handled as sources in the discretized equations. The performance of the numerical scheme in 1D and 2D was favourably checked on the basis of classical shallow-water tests, like the spread of several kinds of smooth or steep water bumps, and the dam-break problem (Delis and Katsaounis, 2005) (tests not shown).

Fig. 7 shows the simulated water depth at the northeasterly boundary of the domain, that is, at the entrance of the Ciutadella inlet. Note that this output, as it is shown, already includes the contribution due

⁴ This is an appropriate framework for our problem because the “shallow depth” assumptions are fully applicable: water is considered incompressible, viscous effects are negligible and the ocean wave lengths of interest (10–20 km) are much larger than the water depth (< 100 m).

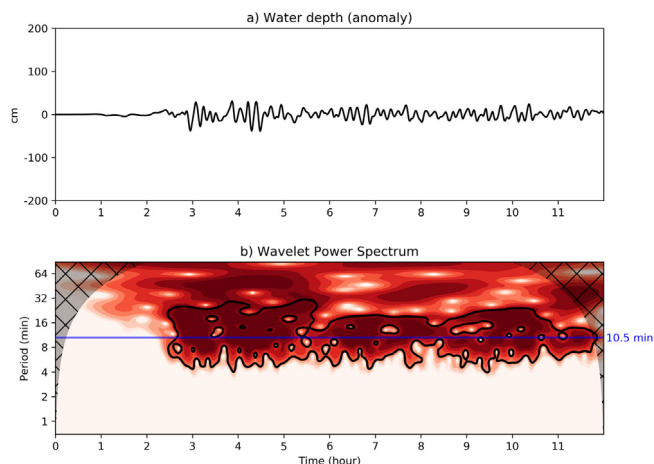


Fig. 7. Ocean model simulation of 21 Jun 1984 case study: (a) Time series of the water depth signal obtained at the end of the Menorca channel (i.e. at the mouth of the Ciutadella harbour); (b) Wavelet power spectrum of the water depth series (the indicated period of 10.5 min, in blue, corresponds to the fundamental period of the harbour seiche).

to wave shoaling; remember this process is parameterized in a very simple way by virtue of Green’s law for an 80 to 5 m change in marine depth: the simulated wave amplitude is artificially doubled before forcing the coastal response in Ciutadella (next section). As expected, for the 21 June 1984 case study the atmospheric forcing and Proudman resonance become instrumental for allowing the ocean waves to gain significant amplitude before impinging Ciutadella. The greatest wave heights are simulated some minutes after $t = 4$ h (Fig. 7a), reaching about 70 cm (shelf amplification included). In addition, the involved wave frequencies (mostly in the range between 6 and 20 min; Fig. 7b) become in principle highly favourable to excite a wide seiche response in the harbour.

2.3. Ciutadella inlet (harbour resonance)

The final step of our numerical method aimed at the prediction of meteotsunamis in Ciutadella is its coastal component, again an idealized framework which operates on a domain 1.1 km long and 5 m deep, quite representative of the inlet geometry (top-left inset in Fig. 1). The same shallow-water model of last section will be applied, but with the frictional force as the only extra term in the momentum equation. The nature of the boundary conditions is obviously different: water depth anomaly is prescribed every 20 s at the SW boundary open to the Menorca channel (this is the output of the preceding ocean model, e.g. Fig. 7a) while rigid wall conditions are assumed at the NE closed end. The simulation is run with a spatial resolution $\Delta x = 12$ m and we are interested in exploring the outcome in terms of the water depth near this latter boundary, where the effect of the harbour resonance would be at its maximum.

Fig. 8 shows the result of the coastal simulation for the 21 June 1984 case study; this can be compared with the input forcing that was shown in Fig. 7. Substantially amplified seiches (i.e. rissaga oscillations) are obtained at the harbour. As it could have been anticipated from previous steps of the prognostic chain, the largest of these meteotsunamis is found at around $t = 4.5$ h (Fig. 8a) with a calculated magnitude (maximum crest-to-trough difference) of 358.3 cm. This means an extraordinary meteotsunami in the context of the known climatology, and turns out to be in excellent agreement with the estimated magnitude of this historical event (350 cm). As expected, the energy of the simulated signal is highly focalized around the theoretical fundamental period of the harbour (10.5 min; see Fig. 8b).

On the other hand, a few more lessons on the functionality of the method can be derived solely from the selected case study. First, it is

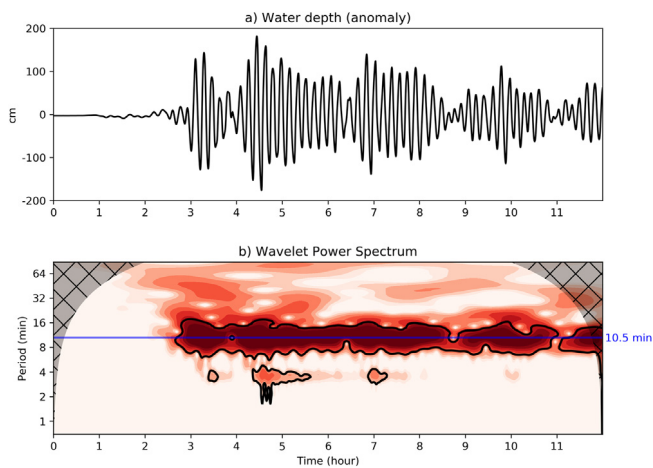


Fig. 8. As in Fig. 7, but corresponding to the coastal model simulation at the end of the Ciutadella harbour.

interesting to analyse what would have been the outcome if instead of feeding the technique with the original sounding, we would have used the modified soundings that led to the atmospheric simulations of Figs. 4b and c. For these no-shear and standard lapse-rate soundings we find, respectively, a maximum harbour oscillation of only 22.5 and 7.8 cm, that is, no rissaga at all. We also wonder if the current model configuration, without any extra adjustment or filtering criteria, is naturally suited to discard as rissaga situations those environments lacking a substantial background flow from the southwest. Indeed, four additional experiments starting with exactly the same sounding of Fig. 2 but rotating all winds clockwise by 90, 180 and 270 degrees, yield irrelevant oscillations of 13.1, 0.5 and 2.7 cm, respectively.

3. Overall performance of the prognostic system

The potential of the new method has only been demonstrated for a particular – although certainly extraordinary – rissaga event. The idea that extreme manifestations of complex physical processes can be accurately anticipated by a prognostic system, whatever its degree of sophistication, still seems far off. But even a modest skill in identifying (at least qualitatively) a good number of hazardous situations would make of such system a very useful tool, especially when combined with parallel techniques. Of similar relevance is the ability to detect the much more frequent non-hazardous days, in order to keep predicted false alarms within acceptable limits. In this section we analyse these attributes by running our method on a meaningful number of rissaga and non-rissaga days.

3.1. Rissaga events vs. ordinary situations

No systematic database of rissaga cases has been maintained at the Balearic Islands with a full description of the episodes (e.g. time of the day exhibiting the maximum oscillation, measured wave height, etc.). Except for the last years, when proper measuring devices have been in operation in Ciutadella harbour, or for a few cases which happened during special field campaigns, there is no practical way of reconstructing these quantitative details. Nevertheless, thanks to different sources (these are acknowledged at the end of the document) we were able to compile a list of 128 events, with a mere indication of the meteoevent date and estimated magnitude. For two of the dates no sounding data from Palma was available, so the final list is reduced to 126 rissaga events, extending heterogeneously from July 1981 to July 2018 (plus one old case from September 1975). By definition, these events refer to oscillations greater than 70 cm (this is the conventional threshold for a seiche to be classified a rissaga). It

should be taken into account that in many cases, especially from the 80s and 90s, the assigned magnitude is inherently uncertain for being based on newspaper news or testimonies from witnesses. Despite all these limitations, this dataset seems enough for our purposes.

Each of the 126 rissaga days was submitted to our modelling system, starting – except for possible gaps – with the three operational Palma soundings launched at 00 and 12 UTC on the same day, and at 00 UTC the next day. The harbour seiche of greatest amplitude is chosen from these simulations; recall that the time of the observed event is generally unknown. Fig. 9 displays simulated vs. observed wave heights (red dots). Ideally, these points would lie close to the diagonal. We find substantial spread in the results but there is a general tendency of the sample to draw a growing profile, and about two-thirds of the simulated events contain errors within the ± 50 cm interval. The point labelled as A in Fig. 9 corresponds to the already discussed outstanding forecast of the 21 June 1984 historical event. On the contrary, two particular outliers stand out in the graph: the severe under prediction of the 15 June 2006 record meteoevent (labelled as B) and the extreme overestimation of the moderate rissaga of 8 May 2015 (point C). A plausible explanation for the 15 June 2006 miss is the fact that the current version of our atmospheric model does not include moist processes and therefore cannot simulate pressure jumps linked to the genesis and propagation of convective systems, whereas the observational evidence confers a leading role to convection on that day (Jansà et al., 2007). The 8 May 2015 outlier would deserve special investigation. The responsible Palma sounding at 00 UTC (not shown) reveals extreme south-westerly winds throughout the full troposphere except near the surface, with abnormally large speeds of up to 95 kt around 300 hPa, implying high shear underneath. These features appear to have been critical for the atmospheric simulation, which implicitly assumes the meteorological conditions reflected in a sounding are settled during several hours over the western Mediterranean. However, the thermal and wind profiles appear to have evolved very rapidly on that day as indicated by the observed sounding at 12 UTC, which reveals upper-tropospheric winds of around 80 kt and produces a simulated rissaga of 134 cm, much closer to the observed magnitude of 104 cm.

On average the rissaga prediction system is well calibrated, as indicated by the mean simulated wave height of 119.6 cm, to be compared with the observed mean value of 120.8 cm. In terms of correlation, the results of Fig. 9 do not endorse a very high quantitative correspondence between OBS and SIM. The calculated linear correlation coefficient (0.264) indicates a moderate association; if the two discussed outliers are omitted from the population, this correlation coefficient increases to 0.393.

In second place, a contrasting set of non-rissaga days (maximum harbour oscillations below 70 cm) were simulated. Thanks to the official institution “Ports de Balears”, observed values in this case correspond to actually measured data at the site (1 min resolution series). In particular, we considered the quasi-continuous record from December 2016 to July 2018. After filtering out a dozen of rissaga days happened in that period -these are included in the previous rissaga dataset- and discarding those days without thermodynamic soundings available, we ended up with a substantial set of 549 non-rissaga days. These days were simulated using the closest sounding to the moment of the observed maximum 10 min oscillation. The results are displayed in Fig. 9 using black dots. We observe some tendency of the prognostic system to overestimate the magnitude of many ordinary situations. In fact, 7% of the simulations entail maximum oscillations with errors greater than +50 cm. But in fairness, most of the points appear well clustered near the origin. In terms of averages, the simulated mean oscillation is 25.1 cm, slightly above the observed mean of 17.8 cm. The correlation coefficient between simulated and observed values for the non-rissaga set is 0.428.

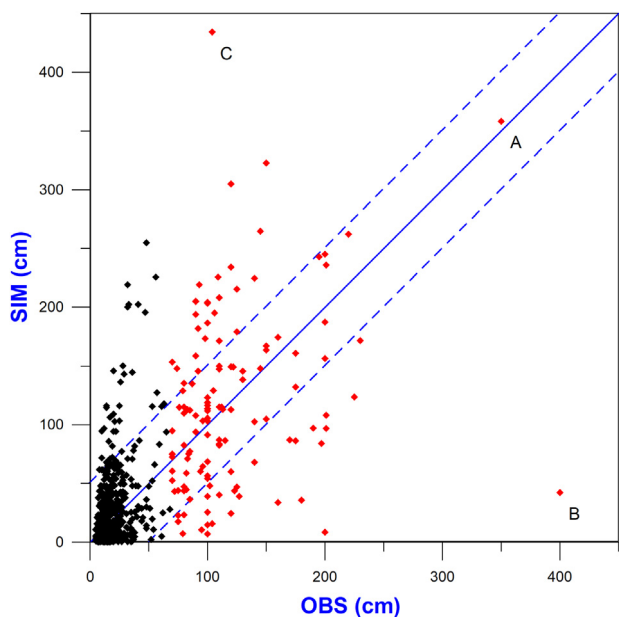


Fig. 9. Global results of the prognostic method: Simulated against observed water oscillations are represented for the 126 rissaga events (red dots) and 549 ordinary cases (black dots). Dashed lines next to the diagonal encompass the ± 50 cm limits. The red dot indicated by “A” letter corresponds to 21 Jun 1984 case study, while the two evident outliers “B” and “C”, discussed in the text, correspond to 15 Jun 2006 and 6 May 2015 events, respectively.

3.2. Summary for categories of practical interest

Overall, the results shown in Fig. 9 are quite encouraging with regard to potential applications of the forecasting system for the automatic identification of rissaga prone situations and even for the issue of special warnings about the risk of large meteotsunamis. Operationally speaking, this kind of quantitative forecasts (necessarily uncertain) are only of relative importance compared to the skill of the system to categorize the daily predictions according to a risk scale of practical interest. In this sense, it has been customary for the Ciutadella harbour to apply the five following forecasting categories⁵: *weak* oscillations (wave heights < 20 cm), *moderate* oscillations (20–70 cm), *rissaga* (70–100 cm); *intense rissaga* (100–200 cm); and *extreme rissaga* (wave height > 200 cm). The first class identifies the most common state of the harbour waters, which are constantly oscillating at the fundamental frequency of the inlet. These oscillations might occasionally reach remarkable although non-hazardous amplitudes (second class) and only beyond the arbitrary limit of 70 cm (rissaga definition) some impacts on the port activities can be expected. In our specific case, 382 and 167 days out of the whole set of 549 ordinary situations belong to the first and second categories, while the 126 rissaga days are distributed as follows: 44 basic rissaga cases, 70 intense events and 12 extreme meteotsunamis. It should be noted that in terms of verification, the narrow limits that define the third class pose some challenges to any predictive system, as individual forecasts can easily fall within contiguous categories.

We first raise the question of “what percentage of the events are correctly forecast by the prognostic system?” (Table 1). Looking at the table, we note as a positive characteristic the quasi-diagonal pattern of the matrix. Non-rissaga days will be correctly forecast most of the times: on weak days (first class) false alarms occur with a percentage less than 3% (yellow, orange and red levels taken together); on moderate days (second category) the chance of issuing an incorrect

⁵ These same categories are used by the AEMET and BRIFS forecasting systems mentioned in the Introduction section.

Table 1

Global performance of the prognostic method in terms of five categories of practical interest for Ciutadella harbour: GREY (weak oscillations, $H < 20$ cm); GREEN (moderate oscillations, 20–70 cm); YELLOW (rissaga, 70–100 cm); ORANGE (intense rissaga, 100–200 cm); and RED (extreme rissaga, $H > 200$ cm). For each observed class (rows) the percentage frequency of each possible forecast (columns) is indicated, thus the table answers the question “What fraction of the events are correctly forecast?”.

		FORECAST (%)				
		GREY	GREEN	YELLOW	ORANGE	RED
OBSERVED	GREY	71.2	25.9	1.8	1.0	0.0
	GREEN	43.1	38.9	6.0	8.4	3.6
	YELLOW	6.8	29.5	18.2	38.6	6.8
	ORANGE	4.3	21.4	14.3	42.9	17.1
	RED	8.3	8.3	8.3	41.7	33.3

rissaga forecast increases to 18%, the remaining percentage is evenly distributed between the two non-rissaga categories. Regarding the skill of the system when a rissaga is presented (yellow, orange and red rows in Table 1) the phenomenon will have been missed (i.e. an oscillation < 70 cm is predicted) about 15%–35% of the occasions, this level depending on the magnitude of the observed rissaga (the stronger the event, the lower the risk of being undetected by the forecast). It is noteworthy that >60% of significant meteotsunamis (orange and red levels considered together) would have been anticipated by the prognostic system. As expected, a perfect prediction of yellow-level meteotsunamis becomes trickier (only 18.2% in percentage), but if we accept as a valuable guidance of the potential risk a forecast from green to orange (i.e. wave heights around one metre) then the predictive skill increases to 86%.

Additionally, it is also interesting to wonder “what percentage of the forecasts are correct in terms of the considered categories?” (Table 2). We find again the desired broad diagonal disposition of the matrix leading elements, although this table should be analysed with caution because the 126/549 ratio of dataset populations does not reflect the actual climatological frequency of rissaga situations (5–10 cases per year). It is outstanding the ability of the method to produce credible predictions of weak situations (grey and green categories). The results are less robust when a rissaga event is forecasted (yellow, orange and red rows in Table 2); in consistency with Fig. 9 we observe that a significant fraction of these forecasts (approx. 25%) will end up as false alarms. Nevertheless, the fraction of hits is remarkably high, especially if we accept the adjacent categories as a suitable domain for verification.

The elements of the above matrices can be further processed to build SIM-OBS contingency tables for categorical forecasts of interest, and from these, to derive commonly used verification indices (e.g. Wilks, 2011; Jolliffe and Stephenson, 2012). We specifically consider the following representative scores: Accuracy (ACC), Bias (BIAS), Probability of Detection (POD), False Alarm Rate (FAR) and Probability of False Detection (POFD); a perfect system would exhibit ACC, BIAS and POD equal to 1 and FAR/POFD equal to 0; all scores can range between 0 and 1, except BIAS that has no upper bound. These scores have

Table 2

As in Table 1, but this time expressing for each type of forecast (rows) the percentage frequency of observed categories (columns), thus answering the question “What fraction of the forecasts are correct?”.

		OBSERVED (%)				
		●	●	●	●	●
FORECAST	F	77.5	20.5	0.9	0.9	0.3
	O	51.3	33.7	6.7	7.8	0.5
	R	19.4	27.8	22.2	27.8	2.8
	A	5.7	20.0	24.3	42.9	7.1
	T	0.0	24.0	12.0	48.0	16.0

been computed considering the conventional thresholds that classify an observed or predicted maximum harbour seiche as non rissaga, rissaga, intense oscillation or extreme event (Table 3). Regarding the power of the forecasting system to discriminate between non-rissaga days and rissaga situations (first two columns in the table), the results are in both cases remarkable. Accuracy and Bias are very good; POD exceeds 90% and 70%, respectively, and while FAR is very low for non-events (0.07) and more adverse for rissagas (0.31), the opposite occurs for the POFD index (0.29 and 0.07, respectively). As expected, the skill of the system is significantly degraded when considering its application to intense and extreme events (Table 3), but it is nonetheless quite encouraging: ACC is close to 1 in both cases; the BIAS score is greater than 1, especially for the extreme threshold, meaning a tendency to over-forecast these situations; POFD keeps very low; and the POD/FAR ratio keeps decreasing as we shift from left to right in the table. For instance, before extraordinary oscillations above two metres, the prognostic system would exhibit a valuable POD of 33%, but at the expense of many false alarms (FAR = 84%). It should be noted that this category is scarcely populated and thus the statistical significance of these results is rather uncertain.

Finally, it would be interesting to compare the performance of our system with the results offered by other techniques also devised for rissaga prediction in the Balearics: the empirically-based AEMET system and the computationally intensive BRIFS method, both of them briefly described in the Introduction. Unfortunately, no publications exist on the statistical performance of these companion techniques and raw data is not available to allow a strict inter-comparison, but at least some flavour of their behaviour can be distilled from what was recently presented by their authors in a topical conference⁶. A contingency table drawn from a limited sample of AEMET forecasts shows (A. Jansà, personal communication): (i) when moderate (> 30 cm) oscillations were observed, 84% of the forecasts indicated a seiche in excess of such threshold (16% missed the event); (ii) for the 30–75 cm range in particular, 25%, 12% and 63% of the forecasts resulted in under-prediction, correct prediction and over-prediction of this category, respectively; (iii) the observed 75–150 cm category was correctly matched 70% of

the occasions, with an even number of under and over-predictions; and (iv) high-amplitude events (> 150 cm) were correctly anticipated by the AEMET method in only 13% of the cases, although two-thirds of the remaining under-predicted events were forecast in the 75–150 cm rissaga category. With regard to the BRIFS system, the following conclusions can be drawn (B. Mourre, personal communication): (i) BRIFS was able to produce a >3 m oscillation for the dramatic June 2006 meteotsunami event analysed in Renault et al. (2011); (ii) the model clearly shows a tendency to underestimate the observed magnitude of the harbour seiches; (iii) in spite of this issue (which is not systematic), during the last four years BRIFS generated significant oscillations (> 0.5 m) in about 75% of observed rissaga events greater than 1 m; (iv) the performance of BRIFS would benefit from more frequent atmospheric outputs used to force the oceanic submodel (1 min frequency or higher) and by using a probabilistic approach built on the basis of multi-physical parameterization schemes in the WRF model, although the computational burden of these measures prevents, for the moment, from their operational implementation. All the above results are clear evidences of the very challenging nature of producing accurate meteotsunami predictions, especially for the most extreme, high-impact cases.

4. Conclusions and future lines of work

The current study proves that basic knowledge of the leading atmosphere–ocean generation mechanisms, along with its plain translation into simple but physically realistic numerical models, is a practical shortcut for predicting meteotsunamis in Ciutadella harbour. From beginning to end (i.e. from reading atmospheric sounding data to computation of the maximum sea level oscillation) our approach merely takes about 5 min to run in a standard PC cluster, and yet it shows valuable skill for the recognition of rissaga risk situations and their classification as weak, moderate or intense. Compared with the application of computationally expensive full models, which at high resolution would require running times of several hours, the new method appears as an interesting supplementary approach. We advocate for the continuous integration of all available rissaga forecasting methods as the ideal operational scenario, that is, an ensemble-based approach.

Our pragmatic approach does not pursue reproduction of actual details of meteotsunami episodes, not only because it focuses exclusively on first order physical processes, but also because it incorporates obvious synthetic elements. In particular, with our strategy aimed at exciting gravity waves in the atmospheric sub model, we do not expect to recreate the observed dynamical evolution. The key idea is to rate the surface pressure anomalies (magnitude and propagation speed) that are allowed by the background environment. The implicit assumption that atmospheric disturbances entering the Balearic region are always guaranteed thanks to some sort of upstream source, as well as the hypothesis of a homogeneous and slowly-evolving background state (reflected in a single sounding) might be questionable in some situations. Future improvements of the technique could take into account the effective onset of gravity waves (e.g. by means of satellite surveillance systems) and should penalize meteorological settings that are forecasted to rapidly evolve from favourable into hostile conditions (e.g. by ingesting time-varying profiles). The versatility of the system could also be improved by a proper recalibration for non-supportive settings (or simply for the cold season as a whole, where rissaga events are unlikely) since we observed a tendency to overpredict the harbour oscillations in these situations. But, above all, the rissaga forecasting system will be benefited by the future inclusion of moist physics in the atmospheric sub model. This is the only way to capture rapid surface pressure fluctuations of convective origin, a relevant player in some Ciutadella meteotsunamis.

Even in its current prototypical version, it is worth testing and adjusting the method for real time operations. With this idea in mind

⁶ The First World Conference on Meteotsunamis (Split, Croatia, 8–11 May 2019).

Table 3

Verification scores (rows, see text) for categorical forecasts (i.e. yes/no) corresponding to the four rissaga classes indicated (columns).

Score	NON RISSAGA (H < 70 cm)	RISSAGA (H ≥ 70 cm)	INTENSE (H ≥ 100 cm)	EXTREME (H ≥ 200 cm)
ACC	0.89	0.89	0.89	0.96
BIAS	0.99	1.04	1.16	2.08
POD	0.93	0.71	0.62	0.33
FAR	0.07	0.31	0.46	0.84
POFD	0.29	0.07	0.07	0.03

a web-based forecasting tool was recently implemented⁷. The system provides probabilistic predictions of rissaga risk according to the five category types discussed in last section, considering a time horizon of three days and separate forecasts for early, central and late hours of the day. Input soundings over the Balearics are taken from the hourly predictions of NCEP/Global Forecast System (GFS) model. Each of these soundings (10 for each period of the day) is submitted to the rissaga prognostic method and the modelled maximum oscillations are scrutinized to ascertain the probabilities of each risk level. Thus, we seek to assimilate in this first experimental system the previous notion that there must be a connection between the persistence of a rissaga favourable environment and the probability of finally observing the phenomenon. Additionally, we are currently exploring the application of artificial neural networks (ANN) as rissaga prediction tools. It is expected that a properly trained ANN could not only emulate the expert eye of the human forecaster in detecting the risk of the phenomenon based on the local sounding and the synoptic situation, but also being able to capture those subtleties of the atmospheric state that can lead to intense cases. In particular, the ingestion in the ANN of moisture profiles and convective indices (e.g. CAPE), apart from wind and temperature data, will likely result in an increased versatility of the network.

Another kind of prospective work involves the application of these computationally-efficient techniques as downscaling methods to assess the possible changes in the future risk of meteotsunamis in Ciutadella. The use of fast simulation methods, built on the basis of synthetic-idealized components but including the relevant physics, has proved to be very successful in climate change research. For instance, [Romero and Emanuel \(2017\)](#) applied a statistical-deterministic method to generate from General Circulation Models (GCMs) and at low cost thousands of synthetic storms, with the aim of projecting the future risk of hurricane-like cyclones in the North Atlantic and in the Mediterranean. The method takes advantage of the axisymmetric nature of these cyclones and needs only a 2D framework to adequately model the intensification mechanisms; in addition, an ingredients-based approach was followed to build the synthetic hurricane-prone environments used as input for each considered climate scenario. For the rissaga problem we would need to process a representative large number of daily states provided by the GCMs, both for present and future climatic conditions. Undoubtedly, a prior screening of these states in terms of synoptic-scale proxies recently formulated in connection with the probability of meteotsunami occurrence in the Mediterranean ([Šepić et al., 2016](#); [Vilibić et al., 2018](#)) will help to reduce significantly the number of necessary simulations.

Acknowledgments

We acknowledge four anonymous reviewers for their thorough and useful comments on an earlier version of the study. We would like to thank the “Agencia Estatal de Meteorología” (AEMET, Spain) and our university colleague Prof. S. Monserrat for transferring their lists of “rissaga” events. The public entity “Ports de Balears” is likewise acknowledged for providing high-frequency sea level data recorded at Ciutadella port. All these sources of information were combined to build the observational databases used in Section 3. Atmospheric radio

sounding data from Palma de Mallorca station were extracted from the NCDC/NOAA Integrated Global Radiosonde Archive (IGRA), while plots of particular soundings ([Fig. 2](#)) were obtained from <http://weather.uwyo.edu/upperair/sounding.html>. This research was sponsored by CGL2014-52199-R (EXTREMO) and CGL2017-82868-R (COASTEPS) projects, both of them funded by the Spanish “Ministerio de Economía, Industria y Competitividad, Spain” and partially supported with FEDER, Spain funds. In addition, the leading author developed part of this work while visiting Politecnico di Milano (POLIMI) under Grant PRX17/00007, an action funded by “Ministerio de Educación, Cultura y Deporte” of Spain.

References

- Adams-Selin, R.D., Johnson, R.H., 2010. Mesoscale surface pressure and temperature features associated with bow echoes. *Mon. Weather Rev.* 138, 212–227.
- Bailey, K., DiVeglio, C., Welty, A., 2014. An Examination of the June 2013 East Coast Meteotsunami Captured By NOAA Observing Systems. NOAA Technical Report NOS CO-OPS 079. 42 pp.
- Bubalo, M., Janeković, I., Orlić, M., 2018. Chrystal and proudman resonances simulated with three numerical models. *Ocean Dyn.* 68, 497–507.
- Davies, H.C., Turner, R.E., 1977. Updating prediction models by dynamical relaxation: An examination of the technique. *Q. J. R. Meteorol. Soc.* 103, 225–245.
- Delis, A.I., Katsaounis, Th., 2005. Numerical solution of the two-dimensional shallow water equations by the application of relaxation methods. *Appl. Math. Model.* 29, 754–783.
- Doyle, J.D., Gaberšek, Q., Jiang, L., Bernardet, J.M., Brown, A., Dörnbrack, E., Filaus, V., Grubišić, D.J., Kirshbaum, O., Knoth, S., Koch, J., Schmidli, I., Stiperski, S., Vosper, S., Zhong, S., 2011. An intercomparison of T-REX mountain-wave simulations and implications for mesoscale predictability. *Mon. Weather Rev.* 139, 2811–2831. <http://dx.doi.org/10.1175/MWR-D-10-05042.1>.
- Durrain, D.L., 2010. Numerical Methods for Fluid Dynamics (With Applications to Geophysics), second ed. Springer, 516 pp.
- Giraldo, F.X., Restelli, M., 2008. A study of spectral element and discontinuous Galerkin methods for the Navier–Stokes equations in nonhydrostatic mesoscale atmospheric modeling: Equation sets and test cases. *J. Comput. Phys.* 227, 3849–3877.
- Green, G., 1838. On the motion of waves in a variable canal of small depth and width. *Trans. Cambridge Phil. Soc.* 6, 457–462.
- Hibiya, T., Kajuru, K., 1982. Origin of the Abiki phenomenon (a kind of seiche) in nagasaki Bay. *J. Ocean. Soc. Jpn.* 38, 172–182.
- Jansà, A., Monserrat, S., Gomis, D., 2007. The rissaga of 15 June 2006 in Ciutadella (Menorca), a meteorological tsunami. *Adv. Geosci.* 12, 1–4.
- Jolliffe, I.T., Stephenson, D.B., 2012. Forecast Verification: A Practitioner’s Guide in Atmospheric Science, second ed. John Wiley and Sons, Ltd, 274 pp.
- Kelley, D.E., 2018. Oceanographic Analysis with R. Springer, 290 pp.
- Klemp, J.B., Dudhia, J., Hassiotis, A.D., 2008. An upper gravity-wave absorbing layer for NWP applications. *Mon. Weather Rev.* 136, 3987–4004.
- Leveque, R.J., 2002. Finite Volume Methods for Hyperbolic Problems. Ed. Cambridge University Press, 558 pp.
- Lindzen, R.S., Tung, K.K., 1976. Banded convective activity and ducted gravity waves. *Mon. Weather Rev.* 104, 1602–1617.
- Ličer, M., Murre, C., Troupin, A., Kriemeyer, A., Jansà, B., Tintoré, J., 2017. Numerical study of balearic meteotsunami generation and propagation under synthetic gravity wave forcing. *Ocean Model.* 111, 38–45.
- Marcos, M., Monserrat, R., Medina, A., Orfila, S., Olabarrieta, M., 2009. External forcing of meteorological tsunamis at the coast of the Balearic Islands. *Phys. Chem. Earth* 34, 938–947.
- Monserrat, S., Thorpe, A.J., 1996. Use of ducting theory in an observed case of gravity waves. *J. Atmos. Sci.* 53, 1724–1736.
- Monserrat, S., Vilibić, I., Rabinovich, B., 2006. Meteotsunamis: atmospherically induced destructive ocean waves in the tsunami frequency band. *Nat. Hazards Earth Syst. Sci.* 6, 1035–1051.
- Pattiaratchi, C.B., Wijeratne, E.M.S., 2015. Are meteotsunamis an underrated hazard? *Phil. Trans. R. Soc. A* 373, 20140377.
- Paxton, C.H., Sobien, D., 1998. Resonant interaction between an atmospheric gravity wave and shallow water wave along Florida’s west coast. *Bull. Am. Meteorol. Soc.* 79, 2727–2732.

⁷ See <http://meteo.uib.es/rissaga>.

- Plougonven, R., Zhang, F., 2014. Internal gravity waves from atmospheric jets and fronts. *Rev. Geophys.* 52, 33–76.
- Proudman, J., 1929. The effects on the sea of changes in atmospheric pressure. *Geophys. Suppl. Mon. Notices Royal Astron. Soc.* 2 (4), 197–209.
- Rabinovich, A.B., 2009. Seiches and harbor oscillations. In: Kim, Y.C. (Ed.), *HandBook of Coastal and Ocean Engineering*. World Scientific Publishing Company, Singapore, pp. 193–236.
- Rabinovich, A.B., Monserrat, S., 1998. Generation of meteorological tsunamis (large amplitude seiches) near the Balearic and Krul Islands. *Nat. Hazards* 18, 27–55.
- Ramis, C., Jansà, A., 1983. Condiciones meteorológicas simultáneas a la aparición de oscilaciones del nivel del mar de amplitud extraordinaria en el Mediterráneo Occidental. *Rev. Geofis.* 39, 35–42.
- Renault, L., Vizoso, G., Jansà, A., Wilkin, J., Tintoré, J., 2011. Toward the predictability of meteotsunamis in the Balearic Sea using regional nested atmosphere and ocean models. *Geophys. Res. Lett.* 38 (L10601), <http://dx.doi.org/10.1029/2011GL047361>.
- Robert, A., 1993. Bubble convection with a semi-implicit formulation of the Euler equations. *J. Atmos. Sci.* 50, 1865–1873.
- Romero, R., Emanuel, K., 2017. Climate change and hurricane-like extratropical cyclones: Projections for North-Atlantic polar lows and medicanes based on CMIP5 models. *J. Clim.* 30, 279–299.
- Schär, C., Leuenberger, O., Fuhrer, D., Lüthi, D., Girard, C., 2002. A new terrain-following vertical coordinate formulation for atmospheric prediction models. *Mon. Weather Rev.* 130, 2459–2480.
- Skamarock, W.C., Klemp, J., Dudhia, D.O., Gill, D.M., Barker, M.G., Duda, X.Y., Huang, W., Wang, J.B., Powers, J.G., 2008. A Description of the Advanced Research WRF Version 3. NCAR Technical Note TN-475+STR. NCAR, Boulder, Colorado (USA), 113 pp.
- Stephan, C., Alexander, M.J., Richter, J.H., 2016. Characteristics of gravity waves from convection and implications for their parameterization in global circulation models. *J. Atmos. Sci.* 73, 2729–2742.
- Straka, J.M., Wilhelmson, L.J., Wicker, J.R., Anderson, R.B., Droegemeier, K.K., 1993. Numerical solutions of a non-linear density current: A benchmark solution and comparisons. *Internat. J. Numer. Methods Fluids* 17, 1–22.
- Van Leer, B., 1977. Towards the ultimate conservative difference scheme IV. A new approach to numerical convection. *J. Comput. Phys.* 23, 276–299.
- Vennell, R., 2010. Resonance and trapping of topographic transient ocean waves generated by a moving atmospheric disturbance. *J. Fluid Mech.* 650, 427–442.
- Vilibić, I., 2008. Numerical simulations of the Proudman resonance. *Cont. Shelf Res.* 28, 574–581.
- Vilibić, I., Šepić, J., 2009. Destructive meteotsunamis along the eastern Adriatic coast: Overview. *Phys. Chem. Earth* 34, 904–907.
- Vilibić, I., Šepić, N., Dunić, F., Sevault, S., Monserrat, J., Jordà, G., 2018. Proxy-based assessment of strength and frequency of meteotsunamis in future climate. *Geophys. Res. Lett.* 45, 10501–10508. <http://dx.doi.org/10.1029/2018GL079566>.
- Šepić, J., I. Vilibić, A.B., Rabinovich, Monserrat, S., 2015. Widespread tsunami-like waves of 23–27 June in the Mediterranean and Black Seas generated by high-amplitude atmospheric forcing. *Sci. Rep.* 5, 11682. <http://dx.doi.org/10.1038/srep11682>.
- Šepić, J., Vilibić, I., Monserrat, S., 2016. Quantifying the probability of meteotsunami occurrence from synoptic atmospheric patterns. *Geophys. Res. Lett.* 43, 10377–10384. <http://dx.doi.org/10.1002/2016GL070754>.
- Wertman, C.A., Yablonsky, R.M., Shen, Y., Merrill, J., Kincaid, C.R., Pockalny, R., 2014. Mesoscale convective system surface pressure anomalies responsible for meteotsunamis along the U. S. East Coast on June 13th, 2013. *Sci. Rep.* 4, 7143. <http://dx.doi.org/10.1038/srep07143>.
- Wicker, L.J., Skamarock, W.C., 1998. A time-splitting scheme for the elastic equations incorporating second-order Runge–Kutta time differencing. *Mon. Weather Rev.* 126, 1992–1999.
- Wilks, D., 2011. *Statistical Methods in the Atmospheric Sciences*, third ed. Academic Press (Elsevier), 704 pp.
- Wilson, B., 1972. Seiches. *Adv. Hydroscl.* 8, 1–94.